Electronic properties of MAPbxSn1– xI3 hybrid perovskite alloys: k.p modeling for tetragonal crystal symmetry with C4v point group

I. Saïdi, K. Boujdaria, M. Chamarro, C. Testelin

Electronic properties of $MAPb_xSn_{1-x}I_3$ hybrid perovskite alloys : k.p modelling for tetragonal crystal symmetry with C_{4v} point group

I. Saïdi[1],* K. Boujdaria[1], M. Chamarro[2], and C. Testelin[2]

[1] *Université de Carthage, Faculté des Sciences de Bizerte, LR01ES15 Laboratoire de Physique des Matériaux : Structure et Propriétés, 7021 Zarzouna, Bizerte, Tunisia and*

[2] *Sorbonne Université, CNRS, Institut des NanoSciences de Paris, F-75005, Paris, France.*

(Dated: December 14, 2024)

Abstract

$MAPb_xSn_{1-x}I_3$ alloys are highly promising for photovoltaic, optoelectronic and spintronics applications. Using **k.p** calculations, we derived the fundamental band parameters of these tetragonal hybrid halide perovskites as a function of Pb content (x). Our study focuses on the experimentally confirmed C_{4v} point group structures: P4mm for Sn-rich alloy and I4cm for Pb-rich alloys.

Our theoretical model successfully reproduces the non-monotonic behavior of the band gap and provides detailed insights into the electron, hole, and reduced exciton masses (m_e, m_h and μ). We find that hole masses are slightly larger than electron masses, with both increasing linearly as x rises. At the structural transition ($x = 0.5$) between P4mm and I4cm, we observe a discontinuity in hole masses and a steeper linear increase in Pb-rich structures. The calculated exciton masses show excellent agreement with experimental data across a wide range of alloy compositions.

Additionally, we predict the Landé g-factors for charge carriers (g_e, g_h) and excitons (g_X). For Pb-rich alloys, g_e increases with decreasing band gap energy, while for Sn-rich alloys, g_e decreases. Exciton g-factors g_X are predominantly governed by the large positive g_e values, as the smaller negative g_h values provide minimal compensation. Consequently, g_X is not constant but varies with the band gap, ranging from 2.4 and 4.8 for Pb-rich alloys and from 4.8 and 3.7 for Sn-rich alloys. These results highlight the tunable electronic and spin properties of $MAPb_xSn_{1-x}I_3$ alloys, positioning them as versatile candidates for next-generation device applications.

*Electronic address: `imen.saidimokded@fsb.ucar.tn`

I. INTRODUCTION

Over the past decade, lead halide perovskite semiconductors have emerged as transformative materials for high-efficiency photovoltaic cells [1], optoelectronic devices [2–4] and quantum information technologies [5]. Among these, perovskite solar cells stand out for their ability to outperform the efficiency of conventional semiconductor technologies, marking a breakthrough in renewable energy research. At the heart of this innovation lies methylammonium lead iodide (MAPI), a key organic-inorganic perovskite that adopts a tetragonal structure at room temperature with a direct band gap of 1.6 eV [6]. As temperatures exceed 328 K [7], MAPI transitions to a pseudo-cubic phase [8–10] with a band gap ranging from 1.55 [11] to 1.57 eV [12].

To approach the fundamental Shockley-Queisser efficiency limit of 33.7% for single-junction solar cells, the optimal band gap should be approximately 1.34 eV [13]. Tandem solar cells offer a path to surpass this limit, requiring bottom-cell materials with even lower band gaps ($0.9-1.2$ eV) to harness energy form the wider band-gap ($1.7-1.9$ eV) top layers [14, 15]. Pure tin-based hybrid perovskites, such as pseudo-cubic $MASnI_3$ (MASI), present a promising solution, with a direct band gap of 1.23 eV$-$1.3 eV at room temperature [8, 16]. Substituting lead with tin in MAPI addresses environmental concerns but introduces challenges, including lower power conversion efficiencies [17–19], and reduced chemical stability due to the oxidation of Sn^{2+} and Pb^{2+}.

A potential solution is the partial substitution of lead with tin, yielding alloys like $MAPb_xSn_{1-x}I_3$. Previous studies [20] have demonstrated that these mixed compositions, such as $MAPb_{0.5}Sn_{0.5}I_3$ and $MAPb_{0.75}Sn_{0.25}I_3$, achieve band gaps of 1.17 eV and 1.24 eV, respectively, while balancing stability and performance.

Beyond photovoltaics, lead halide perovskites also show great promise in spintronics [21–23]. These materials exhibit spin-selective optical transitions and tunable spin-orbit coupling (SOC), which can be adjusted by varying the halogen or metal components. Specifically, substituting lead with tin reduces SOC strength, leading to longer spin relaxation times, a key parameter for spintronic devices. Experimental evidence [24] underscores this effect, paving the way for advanced spin-based technologies.

Given the vast potential of MAPI, MASI, and their alloys, a robust theoretical understanding of their electronic properties is crucial. While pure MAPI and mixed tin-lead perovskites ($MAPb_xSn_{1-x}I_3$) have been extensively studied using first-principle techniques [6, 8, 25–41], discrepancies remain between theoretical predictions and experimental results. For instance, experimental data provide values for key parameters such as exciton reduced mass and binding energy [42], but debates persist about carrier effective masses and the non-monotonic relationship between alloy band gaps and Pb content [20, 26, 43–45].

This anomalous band-gap behavior is likely related to a structural phase transition near x = 0.5 [26]. Tin-rich alloys adopt a P4mm tetragonal crystal symmetry (β phase) , while lead-rich compositions adopt an I4cm tetragonal crystal symmetry (α phase). Both phases belong to the C_{4v} point group, which determines the material's Hamiltonian and electronic properties.

In this article, we consider the C_{4v} point group to calculate the fundamental parameters of $MAPbSnI_3$ perovskites. Specifically, we focus on the energy band structure of the tetragonal phases (P4mm and I4cm) within the effective mass approximation. Extending Z. G. Yu's 8-band **k.p** Hamiltonian [46] to a 14-band model, we provide a detailed framework for analyzing these materials. Semi-empirical approaches such as **k.p** [46–51] and tight-binding [52, 53] methods have previously demonstrated their reliability for modeling pure bulk perovskites, nanostructures [54–56], and trends in experimental parameters [57, 58].

The influence of the organic component's orientation on the electronic properties of hybrid perovskites is beyond the scope of this work. Prior studies by Quarti et al. [33] using ab-initio methods have shown that while the alignment of organic molecules affects band splitting in MAPI, including in I4cm structures, it does not significantly alter band-gap energies or effective masses. Based on these findings, we assume fixed and simplified positions for organic cations in the crystal structure.

Using the C_{4v} point group symmetry, we develop a 14-band Hamiltonian to model the electronic band structure around the direct band gap. This approach builds on established methodologies validated for other symmetry groups, such as O_h [49] and D_{4h} [50]. Applying this proven framework to $MAPb_xSn_{1-x}I_3$ halide perovskites, we aim to uncover new pathways for more sustainable photovoltaic cells and electronic devices.

Given the limited experimental data on the electronic properties of SnPb alloys with $\mathbf{C_{4v}}$ crystal structures, our method provides predictive insights into critical parameters, including

the effective masses and Landé g-factors of electrons, holes, and excitons. These predictions shed light on the electronic behavior of these materials as a function of Pb content, offering valuable guidance for future experimental and technological advancements.

The manuscript is organized as follows. In Sec. II, we describe the crystal structures, introduce the theoretical framework and present the computational details used to calculate the band diagrams of the tetragonal mixed tin-lead $MAPb_xSn_{1-x}I_3$ perovskites. In Sec. III, we investigate the impact of partial Pb substitution by Sn on the evolution of the basic band parameters such as the energy band-gap, SOC and band-gap renormalization by the SOC. In Sec. IV, we calculate the effective masses of electrons and holes for C_{4v} symmetry, from which we also calculate the reduced mass of excitons. Finally, we compare our results with existing literature. In Sec. V, we derive the exciton, electron, and hole Landé g-factors for tetragonal perovskites with C_{4v} as the point group, and compare them with results from recent experimental studies. We conclude in Sec. VI.

II. ELECTRONIC STRUCTURE AND SYMMETRY ARGUMENTS

A. Crystal Structures

The hybrid metal halide perovskites are typically represented as AMX_3 where 'A' is a monovalent organic cation, 'M' is a divalent metal cation, and 'X' represents halide anions arranged in an octahedral structure around 'M'. These $[MX_6]^{4-}$octahedra connect at the corners to form a cage structure, with the 'A' cation positioned at the center. The $MAPb_xSn_{1-x}I_3$ alloy has a structure composed of corner-sharing $[Sn_{1-x}Pb_xI_6]^{4-}$ octahedra, where the metal site is randomly occupied by either Sn or Pb atoms (see Figure 1 from Ref. [20]). The substitution of Sn with Pb ions induces a phase transition at room temperature, with minimal impact on the crystal lattice. Starting from the ideal cubic archetype structure ($Pm\bar{3}m$ space group), we define, φ = M−X−M as the tilting angle between adjacent $[MX_6]^{4-}$ octahedra in the AMX_3 structure. For clarity and simplicity, we refer to the ideal structure as the α-phase, representing the undistorted perovskite in a tetragonal symmetry. For $0 < x < 0.5$, the α-phase prevails, while for x > 0.5, the β-phase emerges, marking the first transition. This transition causes the metal octahedra to tilt, reducing the structural symmetry. Although the overall 3D architecture remains unchanged, the tilting can signifi-

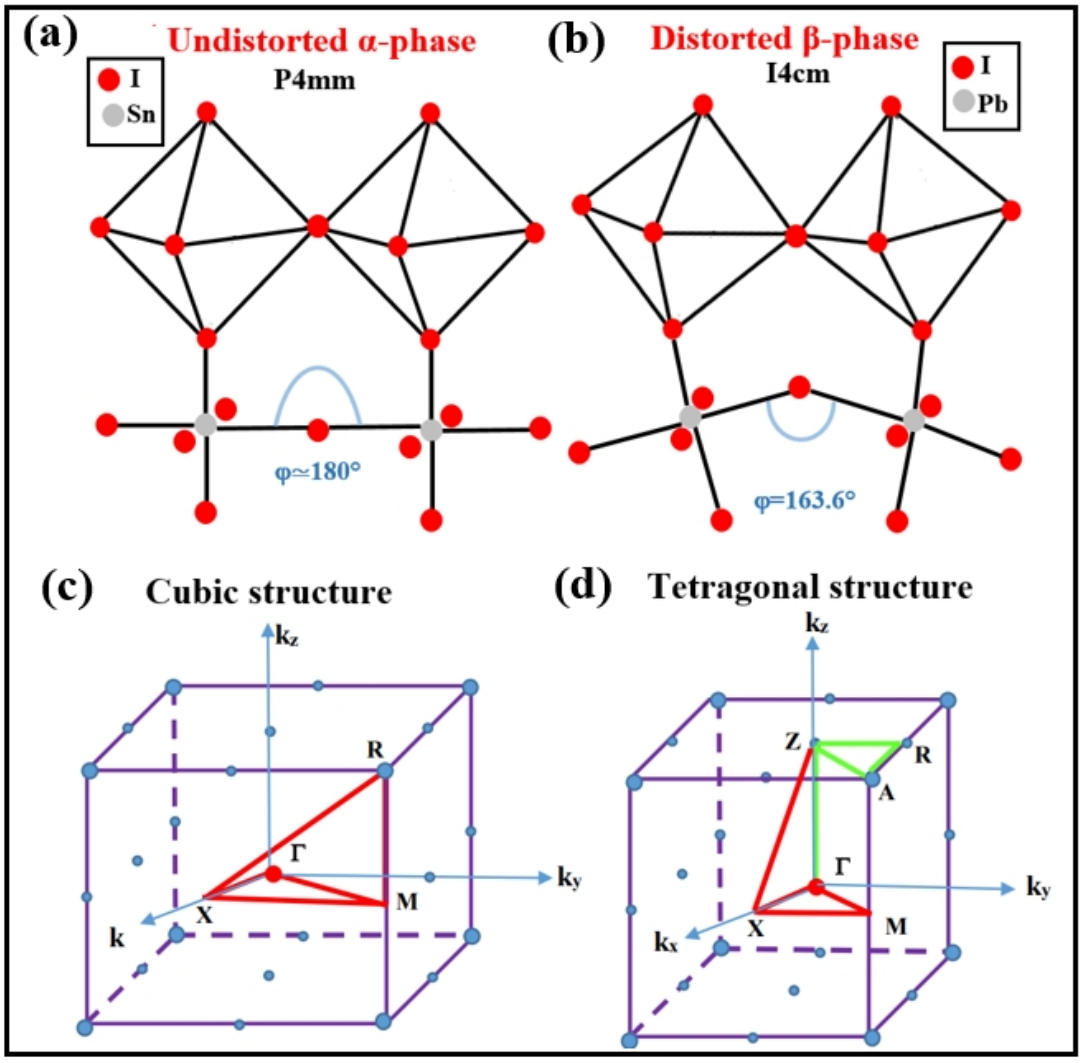

FIG. 1: Crystal structure of halide perovskites AMX_3. The tilting angle φ = M−X−M between adjacent $[MX_6]^{4-}$ octahedra is defined: (a) $\varphi = 177.43°$ in the α-phase for $MASnI_3$ with lattice parameter a = b = 6.230 Å c = 6.232 Å; (b) $\varphi = 163.55°$ in the β-phase for $MAPbI_3$ with a = b = 8.849 Å c = 12.642 Å. Brillouin zone with high symmetry points are described as: $\Gamma(0,0,0)$, $X(0.5,0,0)$, $M(0.5,0.5,0)$, $R(0.5,0,0.5)$ and $\Gamma(0,0,0)$, $X(0.5,0,0)$, $M(0.5,0.5,0)$, $Z(0,0,0.5)$, $R(0.5,0,0.5)$, $A(0.5,0.5,0.5)$ for cubic (c) and tetragonal (d) phases, respectively.

cantly reduce the angle φ from the ideal $\simeq 180°$ for $MASnI_3$ to as low as $\varphi = 163.6°$ in the β-phase [20, 26] as illustated in Figs. 1 (a) and (b).

The Brillouin zones (BZ) and the high-symmetry points, as described in Figs. 1 (c) and (d), highlight the transformation between the cubic and tetragonal structures. This transition includes a 45° rotation and folding of the BZ. For instance, the Γ-M line in the cubic phase transforms the Γ−X line in the tetragonal phase after folding [59]. This transition

is accompanied by the loss of inversion symmetry, which leads to band splitting away from critical points. In the ideal cubic phase, the R-point exhibits a slight band splitting, which becomes more pronounced as it folds onto the A-point in the tetragonal phase. It should be noted that the A-point in the tetragonal phase folds into the Γ-point in the cubic phase, with their respective wave functions undergoing equivalent transformations in the supercell framework. Consequently, the wave function symmetries are preserved, underscoring that the **k.p** model relies exclusively on these symmetries. The specific supercell used in DFT calculations is inherently incorporated within this framework. This effect is particularly significant in the β-phase, where bands are folded from the R-point to the Γ-point [60]. Furthermore, the $\alpha - \beta$ phase transition is associated to a group-subgroup relationship between P4mm and I4cm, which governs the symmetry changes during the phase transition [61].

B. Theoretical Approach

In order to investigate the electronic properties of bulk perovskites $MASn_{1-x}Pb_xI_3$, we utilize the 14-band **k·p** model for the C_{4v} group, which we developed specifically for tetragonal-structured perovskite semiconductors. The s and p valence bands as well as the p conduction bands are part of the 14-band model. A schematic representation near the band-gap of the quantum states involved in the present model is shown in Fig. 2(a). We consider 8 valence band and 6 conduction band states and we incorporate the spin degree of freedom. The band-gap energy, E_G, the energy levels of the second and third conduction bands (E_2, E_3), and the energy levels of the three considered valence bands ($-A_i$ ($A_i > 0$), $i = 1, 2, 3$) are represented in Fig. 2(a). The origin of energies is assumed to be the energy at the top of the higher valence bands (denoted by $|S_V \uparrow (\downarrow)\rangle$ in Fig. 2(a)).

The Bloch functions for the valence bands are represented as s-symmetry orbitals with total angular momentum $j = 1/2$ ($\ell = 0$, ℓ is the orbital angular momentum) and with p-symmetry orbitals having $j = 1/2$ ($\ell = 1$), $j = 3/2$ ($\ell = 1$) (denoted by $|1/2, \pm 1/2\rangle_V$, $|3/2, \pm 1/2\rangle_V$, $|3/2, \pm 3/2\rangle_V$ in Fig. 2(a)). The Bloch functions for the conduction bands have orbital p-symmetry with $j = 1/2$ for the lower conduction bands (denoted by $|1/2, \pm 1/2\rangle_C$ in Fig. 2(a)) and $j = 3/2$ for the upper conduction bands (denoted by $|3/2, \pm 1/2\rangle_C$, $|3/2, \pm 3/2\rangle_C$ in Fig. 2(a)).

We use group theory to directly obtain the effective Hamiltonian describing the studied

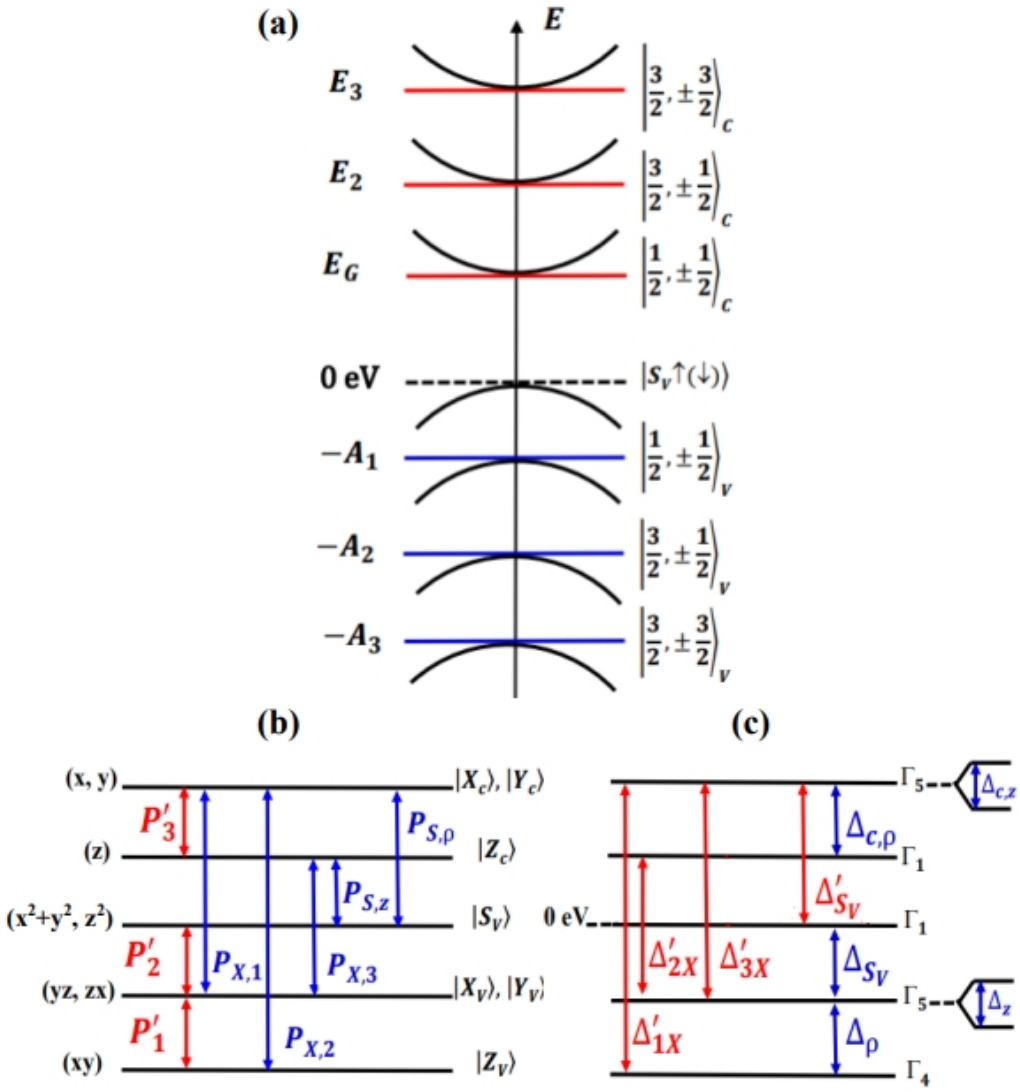

FIG. 2: Band edges, non-zero momentum matrix elements, and effect of spin-orbit interaction in 14-band **k.p** model. (a) 14-band schematic illustrations. We designate the first four double degenerate valence band states as $|S_V\uparrow(\downarrow)\rangle$, $\left|\frac{1}{2},\pm\frac{1}{2}\right\rangle_V$, $\left|\frac{3}{2},\pm\frac{1}{2}\right\rangle_V$ and $\left|\frac{3}{2},\pm\frac{3}{2}\right\rangle_V$. $\left|\frac{1}{2},\pm\frac{1}{2}\right\rangle_C$, $\left|\frac{3}{2},\pm\frac{1}{2}\right\rangle_C$ and $\left|\frac{3}{2},\pm\frac{3}{2}\right\rangle_C$ are the first three double degenerate conduction band states. Horizontal lines are illustrating the band-gap energy, E_G, energy levels of the second and third conduction bands (E_2, E_3), and energy levels of valence bands $(-A_i \ \ (A_i > 0)\,,\ i = 1, 2, 3)$. The energy origin is assumed to be at the top of the upper valence band. (b) The nonzero matrix elements associated to the operator $\mathcal{H}_{\mathbf{k}.\mathbf{p}} = \frac{\hbar}{m_0}\mathbf{k}.\mathbf{p}$ in C_{4v} point group. While the couplings shown in red are specific to the C_{4v} point group and thus zero in D_{4h}, the couplings illustrated in blue are as well nonzero in the D_{4h} point group. (c) Impact of spin-orbit coupling in 14-band C_{4v} point group modeling. The couplings illustrated in red are only found in group C_{4v}, whereas the coupling illustrated in blue are likewise found in group D_{4h}.

system. Proceeding otherwise, i.e. from *ab initio* methods, would lead to very complex calculations, whereas this method has already been proved to be highly effective and efficient in previous works [49, 50]. In the single-group representation (without spin), the data provided in Appendix A show

$$\begin{cases} s_V \sim \Gamma_1 & & \\ p_V\ (X_V, Y_V) \sim \Gamma_5 & , & p_C\ (X_C, Y_C) \sim \Gamma_5 \\ p_V\ (Z_V) \sim \Gamma_4 & , & p_C\ (Z_C) \sim \Gamma_1 \end{cases} \tag{1}$$

The symbol "$\sim$" here indicates how these orbital wave functions change under C_{4v} operations, and the subscripts V and C refer to valence and conduction bands, respectively.

The Bloch theorem is used to generate the effective operator $\mathcal{H}$, which provides the energies of the Bloch envelope functions, following the **k.p** procedure. We write the Hamiltonian as

$$\mathcal{H} = \mathcal{H}_0 + \mathcal{H}_{\mathbf{CF}} + \mathcal{H}_{\mathbf{k.p}} + \mathcal{H}_{\mathbf{SO}} \tag{2}$$

where

$$\begin{cases} \mathcal{H}_0 = \frac{p^2}{2m_0} + \mathcal{U} + \frac{\hbar^2 k^2}{2m_0} \\ \mathcal{H}_{\mathbf{CF}} = T\left[L_z^2 - 2/3\right] \\ \mathcal{H}_{\mathbf{k.p}} = \frac{\hbar}{m_0}\mathbf{k}.\mathbf{p} \\ \mathcal{H}_{\mathbf{SO}} = \frac{\hbar}{4m_0^2c^2}\left(\nabla\mathcal{U} \times \mathbf{p}\right).\sigma \end{cases} \tag{3}$$

Here, m_0 denotes the free electron mass and $\mathcal{U}$ denotes a potential with lattice periodicity. T is the tetragonal crystal field and L_z is the z component of the $\ell = 1$ orbital angular momentum. $\mathbf{p}$ denotes the momentum operator and $\sigma = (\sigma_x, \sigma_y, \sigma_z)$ denotes the standard Pauli spin matrices.

The C_{4v} symmetry group transforms the operator $\mathcal{H}_0$ as Γ_1. The coupling only takes place on the same level. The identity matrix of the representation dimension with the coefficients $\left(E_{\Gamma_m} + \frac{\hbar^2 k^2}{2m_0}\right)$ is proportional to the matrix blocks of $\mathcal{H}_0$.

Equation(3)'s second line gives the Hamiltonian $\mathcal{H}_{\mathbf{CF}}$ in its invariant form [62]. $\mathcal{H}_{\mathbf{CF}}$ describes the crystal field and reflects the impact of distortions undergone by the lattice structure with tetragonal symmetry relative to the cubic structure in the z direction. Alter-

natively, because the lattice constants of the tetragonal phase are frequently within around 1- 3% of those of the cubic α phase, the influence of the tetragonal crystal structure is seen as a simple deformation of the cubic phase's unit cell.

The following selection rule [63, 64] is used to generate the nonzero matrix elements of $\mathcal{H}_{\mathbf{k.p}}$ and $\mathcal{H}_{\mathbf{SO}}$: if the direct product $\Gamma_r \otimes \Gamma_s \otimes \Gamma_t$ includes the unit representation, which is Γ_1 in the C_{4v} point group, then for $|\varphi_r\rangle$ (respectively $\mathcal{O}_s$ and $|\phi_t\rangle$) of symmetry Γ_r (respectively Γ_s and Γ_t), the matrix elements of the $\mathcal{O}_s$ operator, namely $\langle\varphi_r| \mathcal{O}_s |\phi_t\rangle$, are nonzero. The different expressions of the nonzero matrix elements for the last two components of the Hamiltonian $\mathcal{H}$, namely the $\mathbf{k.p}$ and spin-orbit terms, are given in Appendix B. Figures 2(b)-2(c) show schematically the nonzero matrix elements of $\mathcal{H}_{\mathbf{k.p}}$ and $\mathcal{H}_{\mathbf{SO}}$. The couplings specific to only the C_{4v} point group are shown in red, those common to both C_{4v} and D_{4h} point groups are shown in blue.

C. Computational Method

Based on theoretical and experimental studies [20, 42, 43, 65–68], we consider a P4mm (I4cm) crystal structure for alloys with $0 \leq x < 0.5$ ($0.5 < x \leq 1$) , and we use the high symmetry points of the BZ relevant for each considered phase as as described in Fig. 1 (d). We numerically applied the presented $\mathbf{k.p}$ model along with the specified parameter set to calculate the band structures. These parameters can be classified into two categories: input parameters and fitting parameters. The first category contains the energy levels of the three first conduction band states (E_G, E_1, E_2), the energy levels of the p-like valence band states (A_i, i = 1, 2, 3), the tetragonal crystal field T, and the phase angle θ. The energy of the highest valence state is chosen as the origin. In practice, the band-gap energy E_G is fine-tuned to align closely with experimental results [20, 42, 43, 65–68]. The energies E_1, E_2 and A_i are accurately adjusted by comparing the energy band structure obtained from the current model with those predicted by DFT theory calculations [26]. The relationship $\tan(2\theta) = \frac{2\sqrt{2}\Delta_{SO}}{\Delta_{SO}-3T}$ defines the phase angle θ (with $0 < \theta < \frac{\pi}{2}$) [69], linking the band parameters Δ_{SO}, T and θ. Upon using C_{4v} as the point group to generate the tetragonal perovskite's band diagram, θ is crucial in determining the basis on which we express the Hamiltonian $\mathcal{H}$. The phase angle is obtained using the approach outlined in Ref. [50] and adjusted to be close to experimental values [42, 65–68] while fitting the band dispersion. The

crystal field parameter is adjusted to estimate Δ_{SO} through the relationship between Δ_{SO}, θ and T. Our analysis is limited to the SOC interactions within the p conduction bands, under the assumption that the contributions from other SOC components have negligible or no effect on the band dispersion. The second category of fitting parameters includes the remaining parameters listed in Table II of Appendix C, which correspond to the energies associated with the relevant matrix elements of the $\mathcal{H}_{\mathbf{k}.\mathbf{p}}$ Hamiltonian. When fitting the Kane energies ($E_{P_{S,\rho}} = (2m_0/\hbar^2)\, P_{S,\rho}^2$, $E_{P_{S,z}} = (2m_0/\hbar^2)\, P_{S,z}^2$) and other energies like $E_{P_{X,i}} = (2m_0/\hbar^2)\, P_{X,i}^2$ $(i = 1, 2, 3)$ and $E'_{P_i} = (2m_0/\hbar^2)\, P_i'^2$, the effective masses of the carriers and exciton, along with the g-factors of the carriers and exciton, are considered. We observe that, to accurately reproduce the band structure and improve the agreement between theory and experiment, the band parameters are adjusted iteratively. This adjustment strategy is concretely demonstrated through numerical simulation. To calculate the electronic structure and determine various band parameters, we developed a numerical code using MATLAB. Our theoretical model employs a **k.p** approach with 14 bands. By diagonalizing the complete 14×14 matrix, we obtain the eigenvalues, which are then plotted as a function of the wave vector $\mathbf{k}$ in four directions, selecting the relevant BZs based on the crystal symmetry under study.

The electronic band diagrams of C_{4v} tetragonal MASI ($x = 0$ composition) and tetragonal MAPI ($x = 1$ composition) are shown in Fig. 3. We observe that the two materials have a direct band gap character that manifests at two distinct locations inside the BZ: for MASI (see Fig. 3(a)), at A point, and for MAPI (see Fig. 3(b)), at Γ point which is the center of the BZ. We have used the data provided in [26] as a reference for our calculations of the band diagram of $MAPb_xSn_{1-x}I_3$ compounds with P4mm or I4cm as a space group and C_{4v} as a point group. Im et *al.* [26] employed first-principles density functional theory (DFT) using the projector-augmented wave method [70], to calculate the electronic structures of $MASn_{1-x}Pb_xI_3$, implemented in Vienna Ab Initio Simulation Package [71]. The exchange-correlation functional was treated by the generalized gradient approximation (GGA) within Perdew-Burke-Ernzerhof (PBE) formalism [72] for structural relaxation and basic electronic structure calculation, while for more accurate band gap, they used the hybrid functional within the PBE0 model [73]. SOC has been included. As Fig. 3 illustrates, we obtain an acceptable agreement for $x = 0$ and $x = 1$ with results of Ref. [26]. For alloys, the only theoretical results in the literature are given in Ref. [26] and only report the band-gap

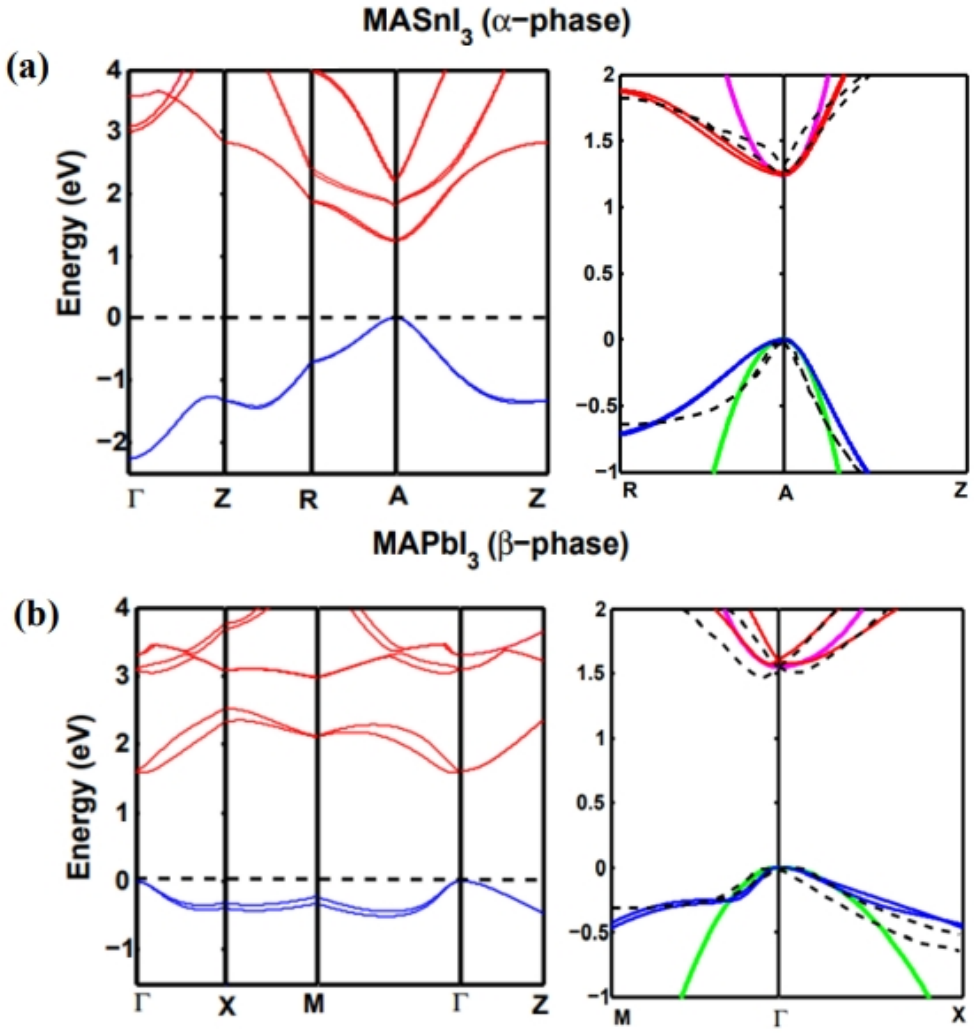

FIG. 3: Left panels: band diagrams, for (a) the bulk tetragonal P4mm space group $MASnI_3$ and (b) the tetragonal I4cm space group $MAPbI_3$ crystal structures. The energy band structures are obtained from the 14-band **k.p** model with a C_{4v} symmetry. Right panels: a comparison between our calculated band structures (red and blue solid lines), those from Ref. [26] calculated by DFT (dashed lines) and parabolas obtained from the fitted effective masses (pink and green solid lines) . The regions around the R→A→Z direction for MASI ((a) right panel) and around the M→ Γ →X direction ((b) right panel) for MAPI have been magnified.

energies. We underline in Fig. 3(b) the presence of a Rashba-type splitting at the Γ point due, according to Ref. [26], to the presence of off-centering Pb atoms in the crystallographic structure and SOC.

To evaluate the extent to which the effective mass approximation applies around the A and Γ points in our approach, we compared our results with parabolas fitted using the effective masses. This allows us to assess the degree of parabolicity: we found this to hold

in a range of $10-20\%$ of the BZ, depending on the specific direction and point considered. Our approach generally yields an acceptable agreement for the energy band structure over a width of approximately 5 eV: 1 eV across the valence band and over a 4 eV scale along four directions of the lowest conduction bands ((ΓZ, ZR, RA, AZ) in α-P4mm phase, (ΓX, XM, MΓ, ΓZ) in β-I4cm phase).

III. BAND GAP ENERGY AND SPIN-ORBIT COUPLING

In Fig. 4(a), the calculated band-gap energy for both α (P4mm) and β (I4cm) phases is plotted versus the Pb content and compared to the theoretical expectations predicted by first-principle calculations [26, 28], as well as experimental measurements [20, 26, 42–44]. DFT and **k.p** theoretical methods give very similar dependences on Pb content and similar values for the band-gap energy. Strikingly, both show a non-linear behavior with Pb content, with the band gaps minimum predicted by both calculations is found for compositions between 0.3 and 0.5 ($0.3 < x < 0.5$). Such a deviation from a simple linear dependence on alloy composition is a common phenomena for semiconductor alloys, but has different microscopic origins in different materials. For halide Pb-Sn-based perovskites, relativistic [26, 74] and steric processes [26, 75], as well as an energy mismatch between the Pb and Sn orbitals [45], have all been suggested as potential origins of this anomalous evolution of the band-gap energy.

We also observe a slight discrepancy c.f. the experimental results. The experimentally obtained band-gap energies exhibit a slight discrepancy that is never larger than 200 meV. This difference may originate from the growth procedures used by different authors to obtain the final alloy and/or from the methods used to experimentally determine this physical quantity. Nevertheless the comparison of **k.p** predictions versus experimental results clearly shows a reasonable agreement. For $x < 0.5$, the band-gap energy is found to decrease linearly as x increases, as the valence band maximum remains practically unchanged, whereas the conduction band minimum decreases linearly in energy. For $x > 0.5$, the increase of Pb content causes the band-gap energy to rapidly grow according to a super-linear behavior.

The SOC energy in MASI is about $\Delta_{SO} = 0.5$ eV, three times smaller than in MAPI. It is clear that there is an increase in the SOC when the Pb atoms substitute the Sn ones. Fig. 4(b) highlights this trend and illustrates the increase of Δ_{SO} as x increases. Δ_{SO} increases

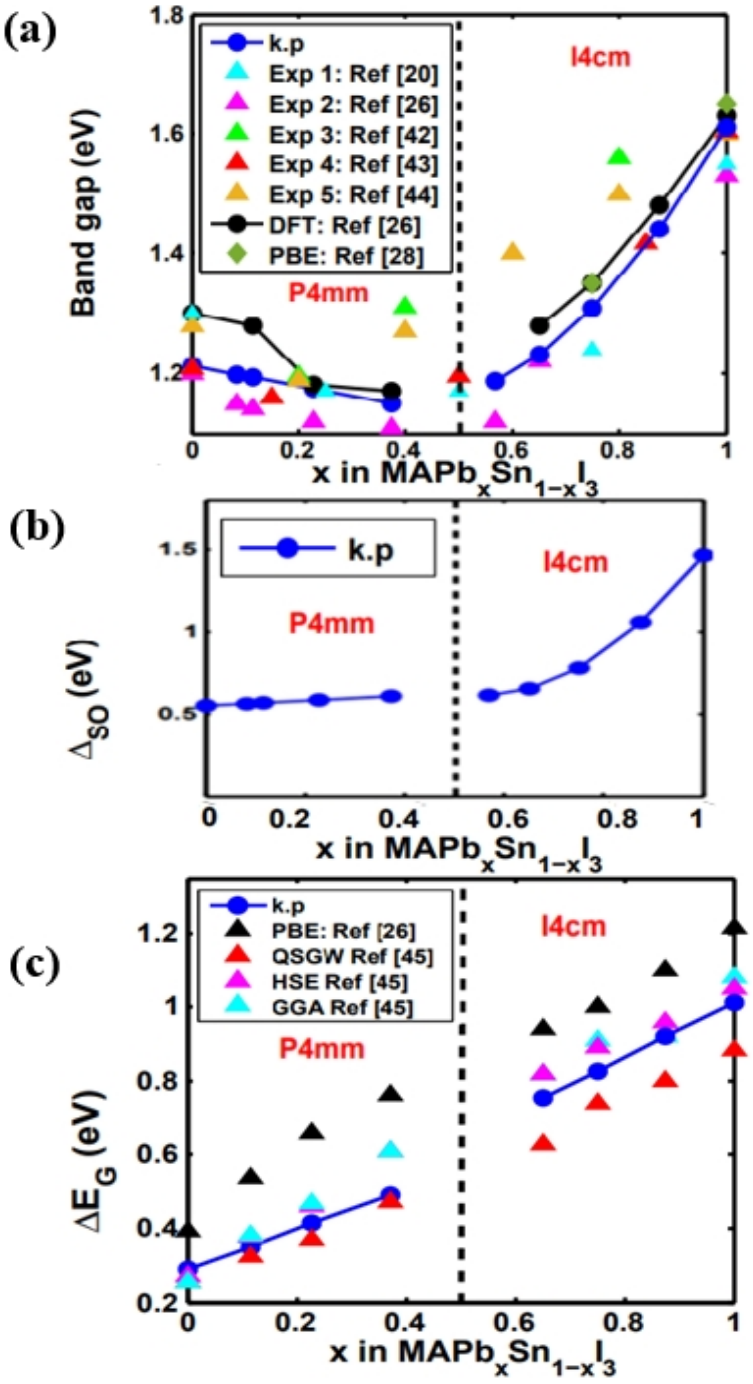

FIG. 4: $MAPb_xSn_{1-x}I_3$ band-gap energy, spin-orbit coupling and band-gap renormalization as a function of lead content. Vertical dashed line corresponds to x=0.5. (a) Evolution of the band-gap energy as a function of x composition; our results are compared with both available experimental and theoretical results. (b) The calculated spin-orbit coupling evolution as a function of x. (c) The band-gap renormalization by spin-orbit coupling as a function of x composition.

linearly and moderately in the α phase, but in the β phase it increases faster according to a quadratic law. The SOC of heavy metals like tin and lead has a significant impact on the electronic structures of halide perovskites at low energies [76]. That is why designing the SOC strength is crucial to control various SOC-associated properties [76, 77], and, in particular, the band-gap renormalization as we will discuss below.

Fig. 4(c) displays the evolution of the band-gap reduction (renormalization) by SOC, ΔE_G, as a function of Pb content, and is compared to previous theoretical predictions [26, 45]. ΔE_G is defined as the difference between the calculated band-gap energies obtained without and with SOC, respectively. The calculated ΔE_G for α and β phases nicely reproduces the band-gap renormalization behavior previous predicted [26, 45]. However, we note that our findings are closer to the results of Ref. [45] than those of Ref. [26]. The results show a linear behavior, ΔE_G being the highest for the highest Pb content.

In the following, we present our findings regarding the effective masses and the Landé g-factors of electrons, holes and excitons. It should be noted that these fundamental parameters are closely related to a set of band structure parameters, such as band-gaps energy and the interband momentum matrix elements, that were described in the previous sections.

IV. EFFECTIVE MASSES OF THE CONDUCTION AND VALENCE BANDS

The carrier mobilities in perovskites solar cells have a major impact on their photovoltaic power conversion efficiency, and are directly related to the carrier's effective masses. The charge transport properties of semiconductors are generally influenced by the effective masses of carriers, and designing optoelectronic devices requires an understanding of how these quantities vary with different chemical compositions. Therefore, we provide the effective mass tensor formulas at the band extremum for bulk perovskites with C_{4v} tetragonal symmetry.

For the holes at the top of the valence band, we obtain

$$-\frac{m_0}{m_{h\parallel}} = 1 - E_{P_{S,z}}\left[\frac{\sin^2\theta}{E_G} + \frac{\cos^2\theta}{E_2}\right] \tag{4}$$

$$\begin{cases} -\frac{m_0}{m_{h\perp}} = 1 - \frac{E_{P_{S,\rho}}}{2}\left[\frac{1}{E_3} + \frac{\sin^2\theta}{E_2} + \frac{\cos^2\theta}{E_G}\right] \\ \qquad\qquad + \frac{E'_{P_2}}{2}\left[\frac{1}{A_3} + \frac{\sin^2\theta}{A_2} + \frac{\cos^2\theta}{A_1}\right] \end{cases} \tag{5}$$

Here $m_{h\parallel}$ ($m_{h\perp}$) represents the hole effective mass parallel to (perpendicular to) the tetragonal **c**-axis. $E_{P_{S,\eta}} = (2m_0/\hbar^2)\, P_{S,\eta}^2$ ($\eta = \rho, z$) and $E'_{P_2} = (2m_0/\hbar^2)\, P_2'^2$ are the related energies to the nonzero matrix elements of the momentum $\mathbf{p}$, namely $P_{S,\eta}$ and P_2' (see Fig. 2(b)). Fig. 2(a) shows the energy denominators in Eqs. (4)–(5), and Table II in Appendix C provides their values.

In the lowest conduction band, the electron effective mass tensor components take the form

$$\frac{m_0}{m_{e\parallel}} = 1 + \sin^2\theta \frac{E_{P_{S,z}}}{E_G} + \cos^2\theta\ E_{P_{X,1}} \left[\frac{\cos^2\theta}{(E_G + A_1)} + \frac{\sin^2\theta}{(E_G + A_2)}\right] \tag{6}$$

$$\begin{cases} \frac{m_0}{m_{e\perp}} = 1 + \frac{\cos^2\theta}{2}\left[\frac{E_{P_{S,\rho}}}{E_G} + E_{P_{X,2}}\left(\frac{\sin^2\theta}{(E_G+A_1)} + \frac{\cos^2\theta}{(E_G+A_2)}\right)\right] \\ \quad + \frac{\sin^2\theta}{2} E_{P_{X,3}}\left[\frac{1}{(E_G+A_3)} + \frac{\sin^2\theta}{(E_G+A_2)} + \frac{\cos^2\theta}{(E_G+A_1)}\right] \\ \quad - \frac{E'_{P_3}}{2}\left[\frac{\sin^2\theta}{(E_3-E_G)} + \frac{\cos^2 2\theta}{(E_2-E_G)}\right] \end{cases} \tag{7}$$

where $E_{P_{X,i}}$ ($i = 1, 2, 3$) and E'_{P_3} are the energies associated with the corresponding interband momentum matrix elements (see Fig. 2(b)). The expressions giving $m_{h\parallel,e\parallel}$ are commun to D_{4h} symmetry, whereas $m_{h\perp,e\perp}$ are specific to C_{4v} one. The $E_{P_{X,i}}$ contributions are nonzero in D_{4h} and therefore in C_{4v}, whereas the E'_{P_3} contributions are zero in D_{4h} and nonzero in C_{4v}.

Equations (4-5) for holes and (6-7) for electrons are implemented to determine the effective masses utilizing the band parameters that were extracted using **k.p** modelling (see Appendix C for further details). The dependence of the effective masses versus the Pb content x is displayed in Fig. 5(a), both along and perpendicular to the tetragonal **c**-axis. MAPI shows the largest masses for both electrons and holes among $MAPb_xSn_{1-x}I_3$ compounds with symmetries P4mm (α-phase) and I4cm (β-phase). The electron and hole masses of MAPI compare well with the average values estimated by DFT (GW+SOC) [35]. In line with earlier predictions [6, 28, 78], m_e is smaller than m_h; however, for $x < 0.5$, $m_{h\parallel}$ shows very similar values to $m_{e\parallel}$. For both carriers, the mass along the **c**-axis is smaller than the perpendicular mass. We observe only one exception for these two last statements regarding $m_{h\perp}$: in the range $0.5 < x < 0.65$ there is a linear increase of the electron and hole masses as x increases, with a steeper slope in the Pb-rich zone. We also underline the discontinuity of the $m_{h\perp}$ effective mass value across the α- to β-phase transition ($x = 0.5$).

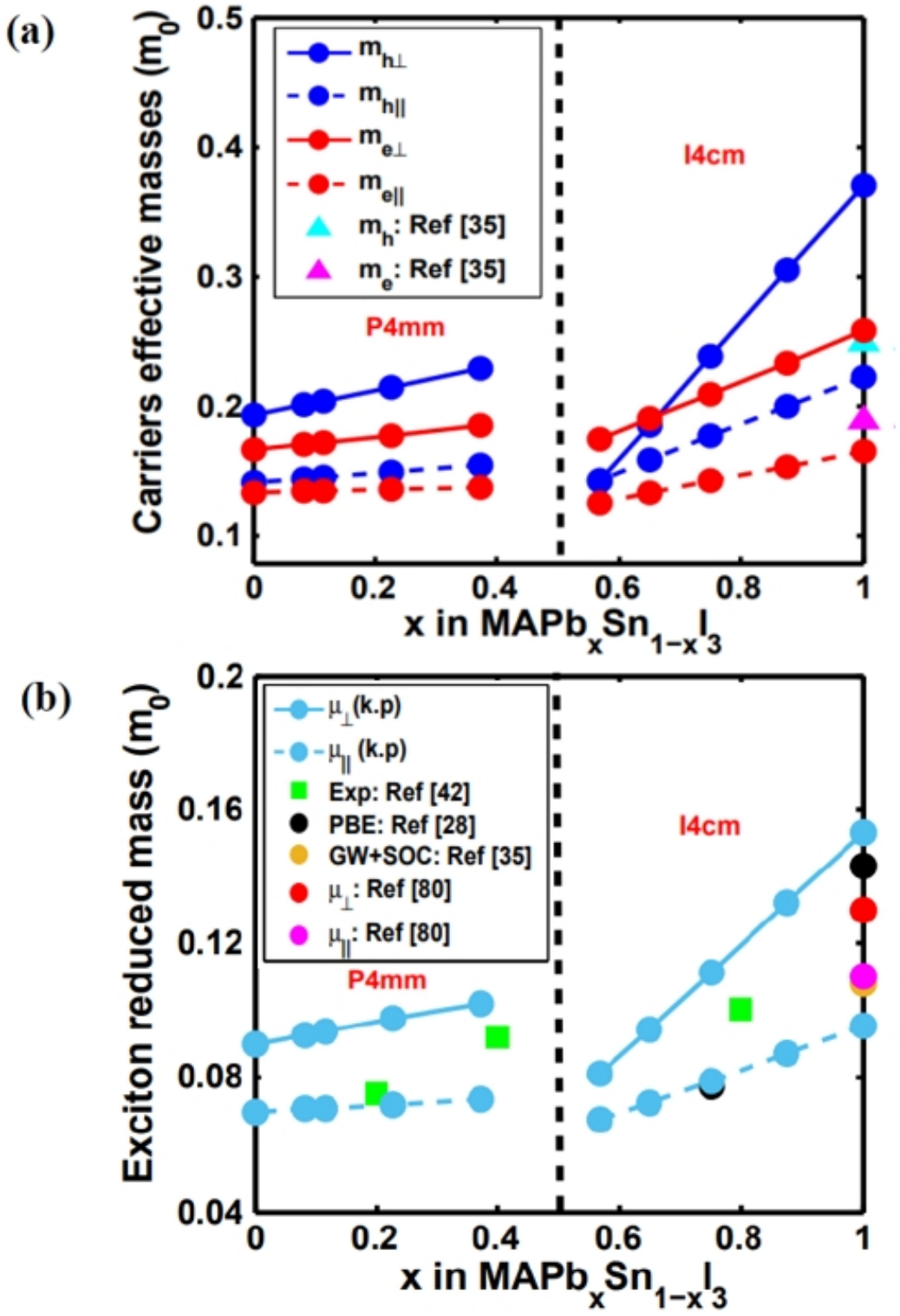

FIG. 5: Dependence of effective masses on lead content. (a) Carriers effective masses obtained from the 14-band **k.p** model for the $MAPb_xSn_{1-x}I_3$ family. (b) We compare our results with available experimental and theoretical data regarding the evolution of reduced exciton mass as a function of x composition.

Knowing that orbital overlap and, consequently, electrical conductivity are optimal when the M-X-M bond angle is least distorted, $MASnI_3$ exhibits greater conductivity than $MAPbI_3$ due to its minimal distortion relative to the ideal configuration [8, 20]. In contrast, $MAPbI_3$, which shows the greatest deviation from the ideal cubic symmetry with a smaller Pb-I-Pb tilting angle, exhibits the lowest conductivity. Indeed, this trend can be extended to carrier mobilities and effective masses. The compound with the highest conductivity possesses the lowest effective masses [79]. This is further confirmed by the fact that the effective mass of $MAPbI_3$ is significantly larger than that of $MASnI_3$. The mixed compositions do not show continuous variation of effective masses as a function of x, as would be expected from a genuine solid solution. In the **k.p** context, the lowest effective masses correspond to compounds exhibiting the strongest coupling between s- and p-valence states and p-conduction states. Specifically, this coupling is associated with the energies ($E_{P_{S,\rho}}$, $E_{P_{X,1}}$) that show a clear increase when transitioning from the P4mm phase to the I4cm at $x = 0.5$.

Fig. 5(b) shows the exciton reduced masses along and perpendicular to the c-axis, noted by $\mu_\parallel$ and $\mu_\perp$, respectively $\left(\mu_\alpha^{-1} = m_{e\alpha}^{-1} + m_{h\alpha}^{-1}, \alpha = \parallel, \perp\right)$. These reduced masses are compared with both experimental [42] and theoretical results [28, 35, 80]. We obtain a reasonable agreement between the experiment and the **k.p** model in a wide range of Pb contents, as shown in Fig. 5(b). Furthermore, the exciton reduced masses obtained from DFT calculations [6, 81], which range from 0.07 m_0 to 0.1 m_0, match well with our results. The compound MASI has the smallest exciton reduced mass in the range ($x < 0.5$), $\mu_{\parallel,\perp}$, and decreases as the tin content increases. Finally, we also observe a discontinuity in the values of the exciton reduced masses at $x = 0.5$, and especially for $\mu_\perp$, as a consequence of the discontinuity previously observed for $m_{h\perp}$.

V. EXCITON, ELECTRON AND HOLE LANDÉ FACTORS

Among the crucial parameters of the conduction and valence states that provide insight into the material's electronic properties are the carrier's Landé factors. Their anisotropy and magnitude governs the coupling of carriers to applied magnetic fields. The Landé factors of carriers for bulk crystals with tetragonal symmetry are anisotropic and may be represented by a second-rank tensors. The g-factor anisotropy provides direct insights into crystal symmetry, especially for the tetragonal symmetry. In this case, the g-factor tensor's element

magnitudes are directly related to the band-gap energy and the interband momentum matrix elements. The Löwdin renormalization [82] and the appropriate matrix elements of the coupling matrix can be used to calculate the elements of the carrier's g-factor tensor.

For the valence band g-factors, a straight forward application of our method has been detailed in Ref. [58] yields

$$\begin{cases} g_{h\parallel} = g_0 + \left[\frac{1}{E_3} - \frac{\sin^2\theta}{E_2} - \frac{\cos^2\theta}{E_G}\right] E_{P_{S,\rho}} - \left[\frac{1}{A_3} - \frac{\sin^2\theta}{A_2} - \frac{\cos^2\theta}{A_1}\right] E'_{P_2} \\ g_{h\perp} = g_0 + \sin\theta\cos\theta\sqrt{2E_{P_{S,\rho}}E_{P_{S,z}}}\left[\frac{1}{E_2} - \frac{1}{E_G}\right] \end{cases} \tag{8}$$

where $g_0 = 2.0023$ is the free electron Landé factor, and $g_{h\parallel}$ ($g_{h\perp}$) is the component of the hole g-factor tensor along (perpendicular) to the **c-**axis of tetragonal structure. Although it is clear that the expression of $g_{h\perp}$ remains to be applicable for D_{4h} and C_{4v}, this is less obvious for $g_{h\parallel}$ because the terms containing E'_{P_2} factor have an intrinsic contribution specific to C_{4v}. It should be noted that the procedure employed here to calculate hole g-factors is the same as the one proposed by L. M. Roth et al. [83] for cubic systems.

The same approach described in Ref . [58] is used to derive the electron's g-factor components. One obtains

$$\begin{cases} g_{e\parallel}^{T-14b} = -2(\cos^2\theta - \sin^2\theta) + \frac{E_{P_{S,\rho}}\cos^2\theta}{E_G} - \frac{E_{P_{X,3}}\sin^2\theta}{(E_G+A_3)} + \frac{E_{P_{X,3}}\sin^4\theta - E_{P_{X,2}}\cos^4\theta}{(E_G+A_2)} \\ \quad + \sin^2\theta\cos^2\theta\frac{E_{P_{X,3}}-E_{P_{X,2}}}{(E_G+A_1)} + E'_{P_3}\left[\frac{\cos^2 2\theta}{(E_2-E_G)} - \frac{\sin^2\theta}{(E_3-E_G)}\right] - 2(1+3\overline{\kappa}_1)\cos^2\theta \end{cases} \tag{9}$$

$$\begin{cases} g_{e\perp}^{T-14b} = -2\sin^2\theta + \sin\theta\cos\theta\frac{\sqrt{2E_{P_{S,\rho}}E_{P_{S,z}}}}{E_G} - \sqrt{2E_{P_{X,1}}E_{P_{X,3}}}\sin\theta\cos\theta \times \\ \qquad \left[\frac{\sin^2\theta}{(E_G+A_2)} + \frac{\cos^2\theta}{(E_G+A_1)}\right] - 2\sqrt{2}\sin\theta\cos\theta(1+3\overline{\kappa}_2) \end{cases} \tag{10}$$

Through the use of Luttinger parameters, $\overline{\kappa}_{1,2}$, the remote band's contributions to the electron Landé factors have been taken into account. Here, $\overline{\kappa}_{1,2}$ are produced by higher-order contributions or coupling between valence and conduction bands other than the ones considered in 14-band model. The parallel component, $g_{e\parallel}^{T-14b}$, has a contribution that is specific to C_{4v} coming from the terms in E'_{P_3}, whilst the perpendicular component $g_{e\perp}^{T-14b}$, continues to be valid for the group D_{4h}. All this comes from the fact that a nonzero matrix element in D_{4h} is always nonzero in C_{4v}. On the other hand, a zero matrix element in D_{4h} can become

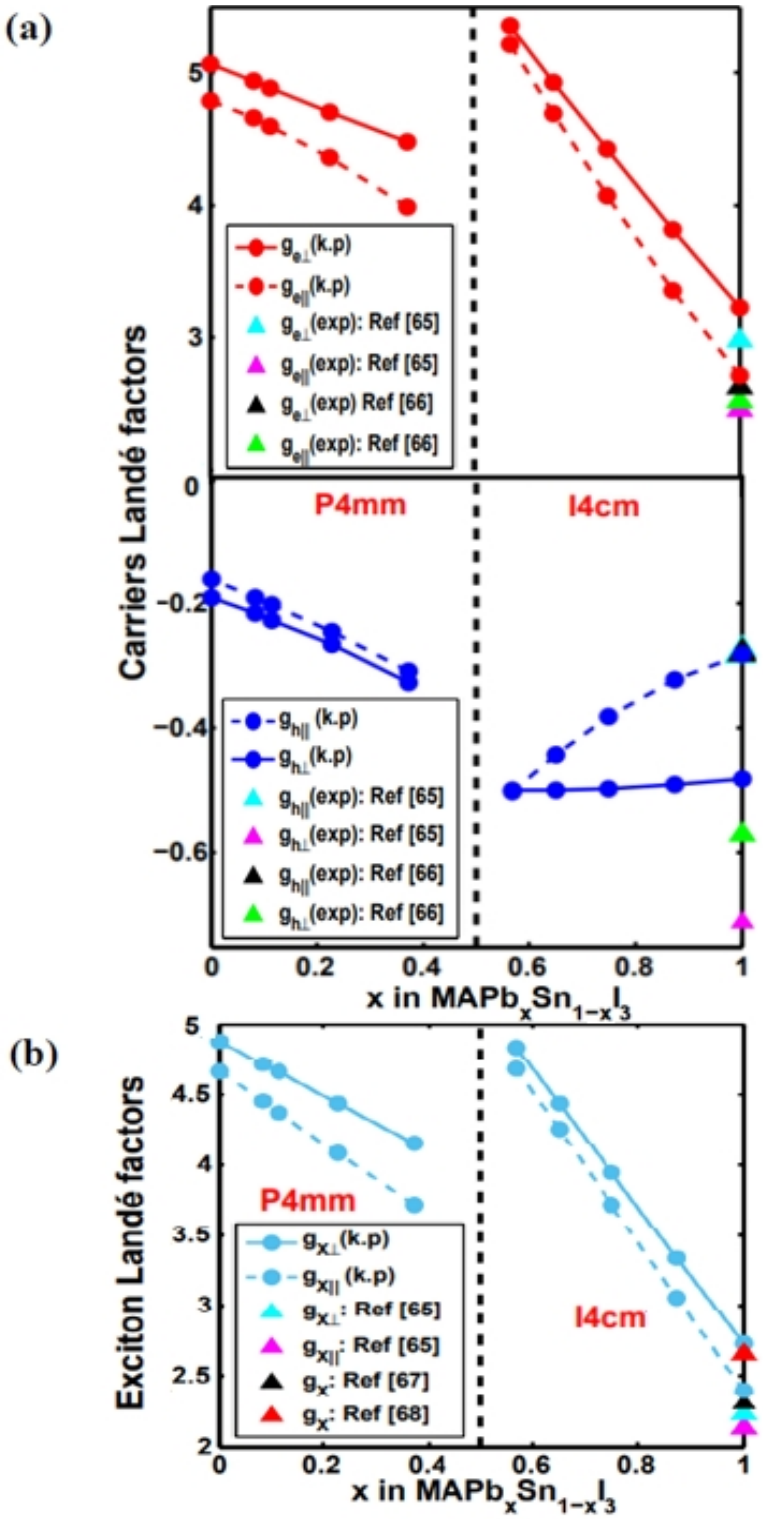

FIG. 6: Carriers Landé factors and exciton Landé factors for $MAPb_xSn_{1-x}I_3$ calculated in the framework of the 14-band **k.p** model by varying the lead content. (a) Tensor of carriers Landé factors evolution as a function of x composition. A comparison with the $MAPbI_3$ experimental results is also shown. (b) Tensor of exciton Landé factors evolution with respect to x. Additionaly presented is a comparison with the experimental data of $MAPbI_3$.

nonzero in C_{4v}.

Knowing the carrier's Landé factors is crucial for guiding future experimental studies and application. In the context of the 14-band **k.p** model, the carrier's Landé factors are determined using Equations (8) for holes and (9-10) for electrons. We have assumed that the remote bands contribution, outside of the 14 bands basis, is negligible ($\overline{\kappa}_1 = \overline{\kappa}_2 = -1/3$). Fig. 6(a) displays the hole and electron Landé factors as a function of Pb composition x. The values obtained for the carrier's g-Landé tensor match the experimental values of MAPI reported in Refs. [23, 65, 66]. One can observe that the g-anisotropy is moderate, as measured on a large range of halide perovskite alloys with $g_{e\parallel} < g_{e\perp}$ and $\left|g_{h\parallel}\right| < |g_{h\perp}|$ [65]. Moreover, the $\left|g_{h\parallel}\right|$ shows values smaller than ($g_{e\perp}$), as previously observed for lead halide perovskites [58, 65]. We underline also in Fig. 6(a), a discontinuity of electron and hole Landé factors values across the crystal structure transition at $x = 0.5$. In the I4cm phase ($x > 0.5$), one observes a slight increase of the hole g-factor and a clear decrease for the electron g-factor as Pb content and E_G increase. Previous experimental results on Pb-based perovskite materials have shown that the value of electron (hole) Landé factors increase (decreases) as the band-gap energy, E_G, decreases from 3.2 eV to 1.5 eV (see Ref. [65]). Here, our results span PbSn alloys, two different crystal structures, and E_G in the 1.1 to 1.6 eV range. We obtain the same E_G-dependence for electron and hole Landé factors for Pb-rich alloys ($0.5 < x < 1$) and I4cm symmetry. However, for Sn-rich alloys and P4mm tetragonal structure (i.e., for $0 < x < 0.5$), both Landé factors decrease as the band-gap energy decreases. This different behavior of the electron Landé factor, compared to Pb-rich compounds, is a consequence of the different electronic band structure.

The sum of the electron and hole g-factors yields the exciton g-factor, g_X, which is a crucial parameter to describe the exciton Zeeman splitting in a magnetic field. Due to the anisotropies of the carrier g-factors, we define the elements of the exciton g-factor tensor as $g_{X\parallel} = g_{e\parallel} + g_{h\parallel}$ and $g_{X\perp} = g_{e\perp} + g_{h\perp}$. Fig. 6(b) shows that $g_{X\perp} > g_{X\parallel}$ with the values of g_X very close to the g_e values. Consequently, we also observe a discontinuity for g_X, exactly as we observed for g_e. In Pb-based halide perovskites covering the band-gap energy range between 1.5 and 3.2 eV, Kopteva et al. [67] have observed a nearly-constant value of g_X ranging between 2.3 and 2.7. The g_X values predicted for MAPI match the experimental data reported in Refs. [65, 67, 68]. For $MAPb_xSn_{1-x}I_3$ alloys with the band-gap energy between 1.1 eV and 1.6 eV, we predict larger g_X values and do not achieve a

nearly-constant value of g_X. This is essentially due the large g_e values in these alloys, which cannot be compensated for by the much smaller (negative) g_h values. For these crucial magnetic properties, there are very few experimental results concerning Pb-Sn based halide perovskites; however, in $MA_{0.3}FA_{0.7}Pb_{0.5}Sn_{0.5}I_3$ polycrystal films at 10K with $E_G = 1.18$ eV (a band-gap value comparable to $MAPb_{0.5}Sn_{0.5}I_3$ [20]), Zhang et al. [84] have obtained $g_e = 4.36$ and $g_h = -0.57$ which leads to $g_X = 3.79$, a value much higher than the highest value obtained in Ref. [67]. For Sn-rich alloys, we predict a slow decrease of g_X as E_G decreases. Our theoretical predictions highlight the peculiar behavior of Pb-Sn based alloys specially for g_X.

VI. CONCLUSION

We have calculated the band structure and fundamental band parameters of $MAPb_xSn_{1-x}I_3$ hybrid perovskites by considering a 14-bands model in the framework of **k.p** theory under the assumption of a C_{4v} point group symmetry. Our calculations show excellent agreement with the experimental non-linear dependence of the band-gap energy with the alloy composition, and are consistent with previous DFT calculations. The tetragonal crystal phase transition between P4mm and I4cm, which has been experimentally observed in $MAPb_xSn_{1-x}I_3$ alloys at $x = 0.5$, leads to a discontinuity of the hole effective mass, $m_{h\perp}$, and the Landé factors g_e and g_h. Consequently, the discontinuity is also present in the exciton reduced mass, μ, and the exciton g-factor, g_X. In good agreement with experimental results, we predict a linear increases of μ with increasing Pb-content. We also predict smaller effective masses along the **c**-axis for both carriers and excitons. For Pb-rich alloys, the predicted values of the exciton Landé factor increase as the band-gap energy decreases and are much larger than those predicted for pure Pb-based halide perovskites. Very recent experiments in $MAFAPbSnI_3$ films fit well with our predictions. All these results show the originality of Pb-Sn based alloys and their promising applications in photovoltaic, opto-electronic and spintronic domains.

APPENDIX

APPENDIX A: D_{4h}-C_{4v} RELATIONSHIPS

Table I provides a summary of the relationships between the C_{4v} and D_{4h} groups in addition to the bases functions for each irreducible representation for the two tetragonal point groups, C_{4v} and D_{4h}.

D_{4h}		C_{4v}	
Bases	Representation	Representation	Bases
$x^2+y^2,\ z^2$	Γ_1^+	Γ_1	$z,\ x^2+y^2,\ z^2$
z	Γ_2^-		
$\mathcal{R}_z$	Γ_2^+	Γ_2	$\mathcal{R}_z$
$z\ \mathcal{R}_z$	Γ_1^-		
x^2-y^2	Γ_3^+	Γ_3	x^2-y^2
$z\ (x^2-y^2)$	Γ_4^-		
xy	Γ_4^+	Γ_4	xy
xyz	Γ_3^-		
$(xz,yz)\,;(\mathcal{R}_x,\mathcal{R}_y)$	Γ_5^+	Γ_5	$(x,y);(\mathcal{R}_x,\mathcal{R}_y);(xz,yz)$
(x,y)	Γ_5^-		

TABLE I: A summary of the correlations between the C_{4v} and D_{4h} point groups. The irreducible representation of the C_{4v} (D_{4h}) point group is denoted by the symbol Γ_n (Γ_m^α). In this Table, bases for each group are also provided. The three Cartesian components of an axial vector are denoted by ($\mathcal{R}_x$, $\mathcal{R}_y$, $\mathcal{R}_z$), whereas the three Cartesian components of an ordinary vector are denoted by (x, y, z).

APPENDIX B: NONZERO MATRIX ELEMENTS of $\mathcal{H}_{\mathbf{k.p}}$ and $\mathcal{H}_{\mathbf{SO}}$

We suggest giving the different formulations of the nonzero matrix elements for the last two components of Hamiltonian $\mathcal{H}$ by starting with $\mathcal{H}_{\mathbf{k.p}}$.

a. Matrix elements of $\mathcal{H}_{\mathbf{k.p}}$

Based on Table I and knowing that the momentum $\mathbf{p}$ is an ordinary vector with three Cartesian components $(p_x, p_y, p_z) \sim (x, y, z)$, we highlight the matrix elements associated

to the operator $\mathcal{H}_{\mathbf{k.p}} = \frac{\hbar}{m_0}\mathbf{k}.\mathbf{p}$. The two transverse components (p_x, p_y) transform as Γ_5 under C_{4v} operations, whereas the longitudinal component p_z transforms as Γ_1. We get an 8 nonzero $\mathbf{k}.\mathbf{p}$ matrix elements (see Fig. 2(b)) based on the group theory rules. Five of them already exist in the D_{4h} point group (illustrated in Fig. 2(b) as blue), while three couplings (shown as red in Fig. 2(b)) are only specific to group C_{4v}.

These are the various nonzero matrix elements' expressions

$$\begin{cases} P_{S,\rho} = (\hbar/m_0)\langle S_V|\, p_x\, |iX_C\rangle = (\hbar/m_0)\langle S_V|\, p_y\, |iY_C\rangle \\ P_{S,z} = (\hbar/m_0)\langle S_V|\, p_z\, |iZ_C\rangle = (\hbar/m_0)\langle iZ_C|\, p_z\, |S_V\rangle \\ P_{X,1} = (\hbar/m_0)\langle X_V|\, p_z\, |iY_C\rangle = -(\hbar/m_0)\langle Y_V|\, p_z\, |iX_C\rangle \\ P_{X,2} = (\hbar/m_0)\langle Z_V|\, p_x\, |iY_C\rangle = (\hbar/m_0)\langle Z_V|\, p_y\, |iX_C\rangle \\ P_{X,3} = (\hbar/m_0)\langle Z_C|\, p_x\, |iY_V\rangle = -(\hbar/m_0)\langle Z_C|\, p_y\, |iX_V\rangle \\ P'_1 = (\hbar/m_0)\langle Z_V|\, p_x\, |iY_V\rangle = (\hbar/m_0)\langle Z_V|\, p_y\, |iX_V\rangle \\ P'_2 = (\hbar/m_0)\langle S_V|\, p_x\, |iX_V\rangle = (\hbar/m_0)\langle S_V|\, p_y\, |iY_V\rangle \\ P'_3 = (\hbar/m_0)\langle Z_C|\, p_x\, |iY_C\rangle = (\hbar/m_0)\langle Z_C|\, p_y\, |iX_C\rangle \end{cases} \tag{B1}$$

While the elements of type P'_j are zero in D_{4h} point group and hence not zero in C_{4v} point group, the matrix elements of type P_j are not zero in either of these two point groups.

b. Spin-orbit coupling

The current procedure ignores the k-dependent spin-orbit term, or $\hbar^2/4m_0^2c^2\,(\nabla\mathcal{U}\times\mathbf{k})\,.\sigma$, and analyzes the effect of spin-orbit interaction only via the following Hamiltonian $\mathcal{H}_{\mathbf{SO}} = \xi\mathcal{G}.\sigma$, where $\xi = \hbar/4m_0^2c^2$ and $\mathcal{G} = (\nabla\mathcal{U}\times\mathbf{p})$. We can deduce that $(\mathcal{G}_x, \mathcal{G}_y) \sim \Gamma_5$ and $\mathcal{G}_z \sim \Gamma_2$ under C_{4v} operations from the fact that $\mathcal{G}$ transforms as $(\mathcal{G}_x, \mathcal{G}_y, \mathcal{G}_z) \sim (\mathcal{R}_x, \mathcal{R}_y, \mathcal{R}_z)$ and knowing that it is an axial vector. There are 9 nonzero spin-orbit interactions terms (see Fig. 2(c)) defined as

$$
\begin{cases}
\Delta_{C,\rho} = -\xi \langle Z_C | \mathcal{G}_x | iY_C \rangle = \xi \langle Z_C | \mathcal{G}_y | iX_C \rangle \\
\Delta_{C,z} = \xi \langle X_C | \mathcal{G}_z | iY_C \rangle = -\xi \langle Y_C | \mathcal{G}_z | iX_C \rangle \\
\Delta_{\rho} = \xi \langle Z_V | \mathcal{G}_y | iX_V \rangle = \xi \langle Z_V | \mathcal{G}_x | iY_V \rangle \\
\Delta_{Z} = \xi \langle X_V | \mathcal{G}_z | iY_V \rangle = -\xi \langle Y_V | \mathcal{G}_z | iX_V \rangle \\
\Delta_{s_V} = \xi \langle S_V | \mathcal{G}_x | iX_V \rangle = \xi \langle S_V | \mathcal{G}_y | iY_V \rangle \\
\Delta'_{1X} = \xi \langle Z_V | \mathcal{G}_x | iY_C \rangle = \xi \langle Z_V | \mathcal{G}_y | iX_C \rangle \\
\Delta'_{2X} = \xi \langle Z_C | \mathcal{G}_x | iY_V \rangle = \xi \langle Z_C | \mathcal{G}_y | iX_V \rangle \\
\Delta'_{3X} = \xi \langle X_V | \mathcal{G}_z | iY_C \rangle = -\xi \langle Y_V | \mathcal{G}_Z | iX_C \rangle \\
\Delta'_{S_V} = \xi \langle S_V | \mathcal{G}_x | iY_C \rangle = \xi \langle S_V | \mathcal{G}_y | iX_C \rangle
\end{cases}
\tag{B2}
$$

Once again, the type Δ_j elements (shown in blue in Fig. 2(c)) are not zero in D_{4h} or C_{4v}, whereas the type Δ'_j elements (shown in red in the Fig. 2(c)) are only zero in D_{4h}.

APPENDIX C: FUNDAMENTAL BAND PARAMETERS VS LEAD CONTENT

Table II provides a summary of the band parameters values that were obtained utilizing the present approach. In general, we found a quadratic dependence with the lead content for the β-phase and a linear dependence in the α-phase.

	α-phase					β-phase				
x_{Pb}	0	0.084	0.115	0.228	0.379	0.569	0.65	0.75	0.875	1
$E_{_G}$ (eV)	1.242	1.238	1.232	1.202	1.158	1.180	1.223	1.286	1.403	1.606
$E_{_2}$ (eV)	1.792	1.80	1.81	1.78	1.76	1.78	1.89	2.09	2.42	3.09
$E_{_3}$ (eV)	2.19	2.17	2.16	2.14	2.11	2.03	2.14	2.35	2.70	3.39
$A_{_1}$ (eV)	0.41	0.44	0.46	0.47	0.48	0.57	0.59	0.60	0.61	0.65
$A_{_2}$ (eV)	0.72	0.71	0.70	0.70	0.70	0.88	0.89	0.82	0.75	0.75
A_3 (eV)	1.04	1.00	0.95	0.94	0.93	1.25	1.24	1.02	0.88	0.79
T (eV)	0	0.041	0.050	0.062	0.075	0.09	0.10	0.18	0.205	0.320
θ $(^\circ)$	35.26	37.23	37.54	38	38.41	37.33	37.85	38.91	39.18	40.01
$E_{P_{S,\rho}}$ (eV)	13.98	13.78	13.58	12.98	11.70	14.38	13.78	12.84	12.48	12.02
$E_{P_{S,z}}$ (eV)	12.65	12.05	11.95	11.40	11.03	11.49	11.50	11.52	11.55	11.92
$E_{P_{X,1}}$ (eV)	7.95	7.86	7.71	7.61	7.21	9.08	8.98	8.88	8.65	6.65
$E_{P_{X,2}}$ (eV)	5.75	5.60	5.52	5.35	5.25	5.18	4.68	4.45	4.28	3.81
$E_{P_{X,3}}$ (eV)	1.68	1.70	1.74	1.88	1.91	1.49	1.43	1.68	1.71	2.04
$E^{'}_{P_1}$ (eV)	0.10	0.11	0.12	0.13	0.12	0.24	0.23	0.22	0.21	0.20
$E^{'}_{P_2}$ (eV)	1.38	1.40	1.44	1.46	1.22	1.50	1.31	1.23	1.18	0.88
$E^{'}_{P_3}$ (eV)	0.02	0.021	0.022	0.024	0.028	1.05	1.11	1.20	1.25	1.85

TABLE II: *A list of the band parameters values that were generated using the current numerical procedure. In general, we found a linear dependence in P4mm symmetry and a quadratic dependence in I4cm symmetry as a function of the lead content.*

ACKNOWLEDGMENTS

This work was financially supported by Tunisian Ministry of Higher Education and Scientific Research, the French Ministry of Foreign Affairs through the project PHC-Utique (CMCU 22G1305), and the French National Research Agency (ANR IPER-Nano2, ANR-18-CE30-0023).

[1] https://www.nrel.gov/pv/cell-efficiency.html

[2] M. V. Kovalenko, L. Protesescu, and M. I. Bodnarchuk, Properties and potential optoelectronic applications of lead halide perovskite nanocrystals, Science **358**,745 (2017).

[3] X-K. Liu, W. Xu, S. Bai, Y. Jin, J. Wang, R. H. Friend, and F. Gao, Metal halide perovskites for light-emitting diodes, Nat. Mater. **20**, 10 (2021) .

[4] H. Wang and D. H. Kim, Perovskite-based photodetectors: materials and devices, Chem. Soc. Rev. **46**, 5204 (2017).

[5] F. Hu, H. Zhang, C. Sun, C. Yin, B. Lv, C. Zhang, W. W. Yu, X. Wang, Y. Zhang, and M. Xiao, Superior optical properties of perovskite nanocrystals as single photon emitters, ACS Nano. **9**, 12410 (2015).

[6] P. Umari, E. Mosconi, and F. De Angelis, Relativistic GW calculations on $CH_3NH_3PbI_3$ and $CH_3NH_3SnI_3$ perovskites for solar cell applications, Sci. Rep. **4**, 4467 (2015).

[7] G. Sharada, P. Mahale, B. P. Kore, S. Mukherjee, M. S. Pavan, C. De, S. Ghara, A. Sundaresan, A. Pandey, T. N. Guru Row, and D. D. Sarma, Is $CH_3NH_3PbI_3$ polar?, J. Phys. Chem. Lett.**7**, 2412 (2016).

[8] C. C. Stoumpos, C. D. Malliakas, and M. G. Kanatzidis, Semiconducting tin and lead iodide perovskites with organic cations: phase transitions, high mobilities, and near-infrared photoluminescent properties, Inorg. Chem. **52**, 9019 (2013).

[9] A. Poglitsch and D. Weber, Dynamic disorder in methylammoniumtrihalogenoplumbates (II) observed by millimeter-wave spectroscopy, J. Chem. Phys. **87**, 6373 (1987) .

[10] Y. Kawamura, H. Mashiyama, and K. Hasebe, Structural study on cubic–tetragonal transition of $CH_3NH_3PbI_3$, J. Phys. Soc. Jpn. **71**, 1694 (2002).

[11] A. Kojima, K. Teshima, Y. Shirai, and T. Miyasaka, Organometal halide perovskites as visible-light sensitizers for photovoltaic cells, J. Am. Chem. Soc. **131**, 6050 (2009).

[12] J. Qiu, Y. Qiu, K. Yan, M. Zhong, C. Mu, H. Yana, and S. Yang, All-solid-state hybrid solar cells based on a new organometal halide perovskite sensitizer and one-dimensional TiO_2 nanowire arrays, Nanoscale. **5**, 3245 (2013).

[13] W. Shockley and H. J. Queisser, Detailed balance limit of efficiency of p-n junction solar cells, J. Appl. Phys. **32**, 510 (1961).

[14] M. T. Hörantner, T. Leijtens, M. E. Ziffer, G. E. Eperon, M. G. Christoforo, M. D. McGehee, and H. J. Snaith, The potential of multijunction perovskite solar cells. ACS Energy Lett. **2**, 2506 (2017).

[15] T. Leijtens, K. A. Bush, R. Prasanna, and M. D. McGehee, Opportunities and challenges for tandem solar cells using metal halide perovskite semiconductors, Nat. Energy. **3**, 828 (2018).

[16] Y. Zhao, J. Wei, H. Li, Y. Yan, W. Zhou, D. Yu, and Q. Zhao, A polymer scaffold for self-healing perovskite solar cells, Nat. Commun. **7**, 10228 (2016).

[17] F. Hao, C. C. Stoumpos, D. H. Cao, R. P. H. Chang, and M. G. Kanatzidis, Lead-free solid-state organic–inorganic halide perovskite solar cells, Nat. Photonics **8**, 489 (2014).

[18] N. K. Noel, S. D. Stranks, A. Abate, C. Wehrenfennig, S. Guarnera, A. A. Haghighirad, A. Sadhanala, G. E. Eperon, S. K. Pathak, M. B. Johnston, A. Petrozza, L. M. Herza, and H. J. Snaith, Lead-free organic–inorganic tin halide perovskites for photovoltaic applications, Energy Environ. Sci. **7,** 3061 (2014).

[19] S. Shao, J. Liu, G. Portale, H.-H. Fang, G. R. Blake, G. H. ten Brink, L. J. Koster, and M. A. Loi, Highly reproducible Sn-based hybrid perovskite solar cells with 9% efficiency, Adv. Energy Mater. **8**, 1702019 (2018).

[20] F. Hao, C. C. Stoumpos, R. P. H. Chang, and M. G. Kanatzidis, Anomalous band gap behavior in mixed Sn and Pb perovskites enables broadening of absorption spectrum in solar cells, J. Am. Chem. Soc. **136**, 8094 (2014).

[21] J. Wang, C. Zhang, H. Liu, R. McLaughlin, Y. Zhai, S. R. Vardeny, X. Liu, S. McGill, D. Semenov, H. Guo, R. Tsuchikawa, V. V. Deshpande, D. Sun, and Z. V. Vardeny, Spin-optoelectronic devices based on hybrid organic-inorganic trihalide perovskites, Nat. Commun. **10**, 129 (2019).

[22] V. V. Belykh, D. R. Yakovlev, M. M. Glazov, P. S. Grigoryev, M. Hussain, J. Rautert, D. N. Dirin, M. V. Kovalenko, and M. Bayer, Coherent spin dynamics of electrons and holes in $CsPbBr_3$ perovskite crystals, Nat. Commun. **10**, 673 (2019).

[23] G. Garcia-Arellano, G. Trippé-Allard, L. Legrand, T. Barisien, D. Garrot, E. Deleporte, F. Bernardot, C. Testelin, and M. Chamarro, Energy Tuning of electronic spin coherent evolution in methylammonium lead iodide perovskites, J. Phys. Chem. Lett. **12**, 8272 (2021).

[24] W. Liang, Y. Li, D. Xiang, Y. Han, Q. Jiang, W. Zhang, and K. Wu, Efficient optical orientation and slow spin relaxation in lead-free $CsSnBr_3$ perovskite nanocrystals, ACS Energy Lett. **6**,1670 (2021).

[25] T. Baikie, Y. Fang, J. M. Kadro, M. Schreyer, F. Wei, S. G. Mhaisalkar, M. Graetzeld, and T. J. Whitec, Synthesis and crystal chemistry of the hybrid perovskite $(CH_3NH_3)PbI_3$ for solid-state sensitised solar cell applications, J. Mater. Chem. A. **1**, 5628 (2013).

[26] J. Im, C. C. Stoumpos, H. Jin, A. J. Freeman, and M. Kanatzidis, Antagonism between spin–orbit coupling and steric effects causes anomalous band gap evolution in the perovskite photovoltaic materials $CH_3NH_3Sn_{1-x}Pb_xI_3$, J. Phys. Chem. Lett. **6**, 3503 (2015).

[27] E. Mosconi, P. Umari, and F. De Angelis, Electronic and optical properties of mixed Sn–Pb organohalide perovskites: a first principles investigation, J. Mater. Chem. A **3**, 9208 (2015).

[28] M-G. Ju, G. Sun, Y. Zhao, and W. Liang, A computational view of the change in the geometric and electronic properties of perovskites caused by the partial substitution of Pb by Sn, Phys. Chem. Chem. Phys. **17**, 17679 (2015).

[29] G. Giorgi, J.-I. Fujisawa, H. Segawa, and K. Yamashita, Small photocarrier effective masses featuring ambipolar transport in methylammonium lead iodide perovskite: a density functional analysis, J. Phys. Chem. Lett. **4**, 4213 (2013).

[30] J. Even, L. Pedesseau, J. M. Jancu, and C. Katan, Importance of spin–orbit coupling in hybrid organic/inorganic perovskites for photovoltaic applications, J. Phys. Chem. Lett. **4**, 2999 (2013).

[31] E. Menendez-Proupin, P. Palacios, P. Wahnon, and J. C. Conesa, Self-consistent relativistic band structure of the $CH_3NH_3PbI_3$ perovskite, Phys. Rev. B **90**, 045207 (2014).

[32] F. Brivio, K. T. Butler, A. Walsh, and M. van Schilfgaarde, Relativistic quasiparticle self-consistent electronic structure of hybrid halide perovskite photovoltaic absorbers, Phys. Rev. B **89**, 155204 (2014).

[33] C. Quarti, E. Mosconi, and F. De Angelis, Interplay of orientational order and electronic structure in methylammonium lead iodide: implications for solar cell operation, Chem. Mater. **26**, 6557 (2014).

[34] A. Stroppa, D. Di Sante, P. Barone, M. Bokdam, G. Kresse, C. Franchini, M. H. Whangbo, and S. Picozzi, Tunable ferroelectric polarization and its interplay with spin–orbit coupling in tin iodide perovskites, Nat. Commun. **5**, 5900 (2014).

[35] A. Amat, E. Mosconi, E. Ronca, C. Quarti, P. Umari, K. Nazeeruddin, M. Grätzel, and A. Filippo De Angelis, Cation-induced band-gap tuning in organohalide perovskites: interplay of spin–orbit coupling and octahedra tilting, Nano Lett. **14**, 3608 (2014).

[36] E. Mosconi, E. Ronca, and F. De Angelis, First-principles investigation of the TiO_2/organohalide perovskites interface: the role of interfacial chlorine, J. Phys. Chem. Lett. **5**, 2619 (2014).

[37] J. Haruyama, K. Sodeyama, L. Han, and Y. Tateyama, Termination dependence of tetragonal $CH_3NH_3PbI_3$ surfaces for perovskite solar cells, J. Phys. Chem. Lett. **5**, 2903 (2014).

[38] A. Buin, P. Pietsch, J. Xu, O. Voznyy, A. H. Ip, R. Comin, and E. H. Sargent, Materials processing routes to trap-free halide perovskites, Nano Lett. **14**, 6281 (2014).

[39] S. X. Tao, X. Cao, and P. A. Bobbert, Accurate and efficient band gap predictions of metal halide perovskites using the DFT-1/2 method: GW accuracy with DFT expense, Sci. Rep. **7,** 14386 (2017).

[40] K. P. Ong, S. Wu, T. H. Nguyen, D. J. Singh, Z. Fan, M. B. Sullivan, and C. Dang, Multi band gap electronic structure in $CH_3NH_3PbI_3$, Sci. Rep. **9**, 2144 (2019).

[41] L. Guan, X. Xu, Y. Liang, S. Han, J. Guo, J. Wang, and X. Li, Effect of atomic configuration on band gap behaviour in $CH_3NH_3Sn_xPb_{1-x}I_3$ perovskites, Phys. Lett. A. **384**, 126173 (2020).

[42] K. Galkowski, A. Surrente, M. Baranowski, B. Zhao, Z. Yang, A. Sadhanala, S. Mackowski, S. D. Stranks, and P. Plochocka, Excitonic properties of low-band-gap lead–tin halide perovskites, ACS Energy Lett. **4**, 615 (2019).

[43] M. Anaya, J. P. Correa-Baena, G. Lozano, M. Saliba, P. Anguita, B. Roose, A. Abate, U. Steiner, M. Grätzel, M. E. Calvo, A. Hagfeldt, and H. Míguez, Optical analysis of $CH_3NH_3Sn_xPb_{1-x}I_3$ absorbers: a roadmap for perovskite-on-perovskite tandem solar cells, J. Mater. Chem. A. **4**, 11214 (2016).

[44] B. Zhao, M. Abdi-Jalebi, M. Tabachnyk, H. Glass, V. S. Kamboj, W. Nie, A. J. Pearson, Y. Puttisong, K. C. Gödel, H. E. Beere, D. A. Ritchie, A. D. Mohite, S. E. Dutton, R. H. Friend, and A. Sadhanala, High open-circuit voltages in tin-rich low-bandgap perovskite-based planar heterojunction photovoltaics, Adv. Mater. **29**, 1604744 (2016).

[45] A. Goyal, S. McKechnie, D. Pashov, W. Tumas, M. van Schilfgaarde, and V. Stevanovic, Origin of pronounced nonlinear band gap behavior in lead–tin hybrid perovskite alloys, Chem. Mater. **30**, 3920 (2018).

[46] Z. G. Yu, Effective-mass model and magneto-optical properties in hybrid perovskites, Sci. Rep. **6**, 28576 (2016).

[47] W. J. Fan, Bulk inversion asymmetry effect on band structure and optical transition of a new class all-inorganic cubic perovskite nanoplatelet, AIP advances **8**, 095206 (2018).

[48] D. Ompong, G. Inkoom, and J. Singh, Effective mass of heavy, light, and spin split-off band electron and hole g-factor in cubic perovskite materials, J. Appl. Phys. **128**, 235109 (2020).

[49] V. Steinmetz, J. Ramade, L. Legrand, T. Barisien, F. Bernardot, E. Lhuillier, M. Bernard, M. Vabre, I. Saidi, A. Ghribi, K. Boujdaria, C. Testelin, and M. Chamarro, Anisotropic shape of $CsPbBr_3$ colloidal nanocrystals: from 1D to 2D confinement effects, Nanoscale **12**, 18978 (2020).

[50] R. Ben Aich, S. Ben Radhia, K. Boujdaria, M. Chamarro, and C. Testelin, Multiband **k.p** model for tetragonal crystals: application to hybrid halide perovskite nanocrystals, J. Phys. Chem. Lett. **11**, 808 (2020).

[51] K. Gawarecki, M. Wiśniewski, M. Polak, R. Kudrawiec, and M. Gładysiewicz, Eight-band **k.p** description and material gain for selected cubic and pseudocubic perovskites, Phys. Rev. Applied **22**, 014058 (2024).

[52] S. Boyer-Richard, C. Katan, B. Traoré, R. Scholz, J.-M. Jancu, and J. Even, Symmetry-based tight binding modeling of halide perovskite semiconductors, J. Phys. Chem. Lett. **7**, 3833 (2016).

[53] M. O. Nestoklon, Tight-binding description of inorganic lead halide perovskites in cubic phase, Comput. Mater. Sci. **196**, 110535 (2021).

[54] S. A. Blundell and C. Guet, All-order correlation of single excitons in nanocrystals using a **k.p** envelope-function approach: Application to lead halide perovskites, Phys. Rev. B **105**, 155420 (2021).

[55] A. Ghribi, R. Ben Aich , K. Boujdaria, T. Barisien, L. Legrand, M. Chamarro, and C. Testelin, Dielectric Confinement and Exciton Fine Structure in Lead Halide Perovskite Nanoplatelets, Nanomaterials. **11**, 3054 (2021).

[56] J. L. Movilla, J. Planelles, and J. I. Climente, Excitons in metal halide perovskite

nanoplatelets: an effective mass description of polaronic, dielectric and quantum confinement effects, Nanoscale Adv. **5**, 6093 (2023).

[57] V. Guilloux, A. Ghribi, S. Majrab, F. Margaillan, M. Bernard, F. Bernardot, L. Legrand, E. Lhuillier, K. Boujdaria, M. Chamarro, C. Testelin, and T. Barisien, Exciton Fine Structure of $CsPbCl_3$ Nanocrystals: An Interplay of Electron-Hole Exchange Interaction, Crystal Structure, Shape Anisotropy, and Dielectric Mismatch, ACS Nano. **17**, 12266 (2023).

[58] G. Garcia-Arellano, K. Boujdaria, M. Chamarro, and C. Testelin, Landé g factors in tetragonal halide perovskite: a multiband **k.p** model, Phys. Rev. B **106**, 165201 (2022).

[59] L. Y. Huang and W. R. L. Lambrecht, Electronic band structure, phonons, and exciton binding energies of halide perovskites $CsSnCl_3$, $CsSnBr_3$, and $CsSnI_3$, Phys. Rev. B. **88**, 165203 (2013).

[60] J. Even, L. Pedesseau, J-M. Jancu, and C. Katan, DFT and **k.p** modelling of the phase transitions of lead and tin halide perovskites for photovoltaic cells, Physica Status Solidi RRL **8**, 31 (2014).

[61] J. Even, L. Pedesseau, C. Katan, M. Kepenekian, J-S. Lauret, D. Sapori, and E. Deleporte, Solid-State Physics Perspective on Hybrid Perovskite Semiconductors, J. Phys. Chem. C. **119**, 10161 (2015).

[62] P. C. Sercel, J. L. Lyons, D. Wickramaratne, R. Vaxenburg, N. Bernstein, and A L. Efros, Exciton Fine Structure in Perovskite Nanocrystals, Nano Lett. **19**, 4068 (2019).

[63] G. Dresselhaus, Spin-Orbit Coupling Effects in Zinc Blende Structures, Phys. Rev. **100**, 580 (1955).

[64] M. S. Dresselhaus, G. Dresselhaus and A. Jorio, Group Theory – Application to the Physics of Condensed Matter, Chap. 6, Springer-Verlag Berlin Heidelberg, (2008).

[65] E. Kirstein, D. R. Yakovlev, M. M. Glazov, E. A. Zhukov, D. Kudlacik, I. V. Kalitukha, V. F. Sapega, G. S. Dimitriev, M. A. Semina, M. O. Nestoklon, E. L. Ivchenko, N. E. Kopteva, D. N. Dirin, O. Nazarenko, M. V. Kovalenko, A. Baumann, J. Höcker, V. Dyakonov, and M. Bayer, The Landé factors of electrons and holes in lead halide perovskites: universal dependence on the band gap, Nat. Commun. **13**, 3062 (2022).

[66] U. N. Huynh, Y. Liu, A. Chanana, D. R. Khanal, P. C. Sercel, J. Huang, and Z. V. Vardney, Transient quantum beatings of trions in hybrid organic tri-iodine perovskite single crystal, Nat. Commun. **13**, 1428 (2022).

[67] N. E. Kopteva, D. R. Yakovlev, E. Kirstein, E. A. Zhukov, D. Kudlacik, I. V. Kalitukha, V. F. Sapega, O. Hordiichuk, D. N. Dirin, M. V. Kovalenko, A. Baumann, J. Höcker, V. Dyakonov, S. A. Crooker, and M. Bayer, Weak dispersion of exciton Landé factor with band gap energy in lead halide perovskites: approximate compensation of the electron and hole dependences, Small. 2300935 (2023).

[68] Z. Yang, A. Surrente, K. Galkowski, N. Bruyant, D. K. Maude, A. A. Haghighirad, H. J. Snaith, P. Plochocka, and R. J. Nicholas, Unraveling the exciton binding energy and the dielectric constant in single-crystal methylammonium lead triiodide perovskite, J. Phys. Chem. Lett. **8**, 1851(2017) .

[69] Y. Nagamune, S. Takeyama, and N. Miura, Exciton spectra and anisotropic Zeeman effect in PbI_2 at high magnetic fields up to 40 T, Phys. Rev. B **43**, 12401 (1991) .

[70] P. Blöchl, Projector Augmented-Wave Method. Phys. Rev. B **50**, 17953 (1994).

[71] G. Kresse and J. Furthmüller, Efficient Iterative Schemes for Ab Initio Total-Energy Calculations Using a Plane-Wave Basis Set. Phys. Rev. B **54**, 11169 (1996).

[72] J. Perdew, K. Burke, and M. Ernzerhof, Generalized Gradient Approximation Made Simple. Phys. Rev. Lett. **77**, 3865 (1996).

[73] C. Adamo and V. Barone, Toward Reliable Density Functional Methods without Adjustable Parameters: The Pbe0Model. J. Chem. Phys. **110**, 6158 (1999).

[74] P. Kanhere, S. Chakraborty, C. J. Rupp, R. Ahuja, and Z. Chen, Substitution induced band structure shape tuning in hybrid perovskites ($CH_3NH_3Pb_{1-x}Sn_xI_3$) for efficient solar cell applications, RSC Adv. **5**, 107497 (2015).

[75] A. Pisanu, A. Mahata, E. Mosconi, M. Patrini, P. Quadrelli, C. Milanese, F. De Angelis, and L. Malavasi, Exploring the limits of three-dimensional perovskites: the case of $FAPb_{1-x}Sn_xBr_3$, ACS Energy Lett. **3**, 1353 (2018).

[76] H. Jin, J. Im, and A. J. Freeman, Topological insulator phase in halide perovskite structures, Phys. Rev. B **86**, 121102(R) (2012).

[77] M. Kim, J. Im, A. J. Freeman, J. Ihm, and H. Jin, Switchable S = 1/2 and J = 1/2 Rashba bands in ferroelectric halide perovskites, Proc. Natl. Acad. Sci. U. S. A. **111**, 6900 (2014).

[78] G. Giorgi, J. I. Fujisawa, H. Segawa, and K. Yamashita, Cation role in structural and electronic properties of 3D organic–inorganic halide perovskites: a DFT analysis, J. Phys. Chem. C **118**, 12176 (2014).

[79] LM. Herz, Charge-Carrier Mobilities in Metal Halide Perovskites: Fundamental Mechanisms and Limits, ACS Energy Lett. **2**, 1539 (2017).

[80] B. Traore, J. Even, L. Pedesseau, M. Kepenekian, and C. Katan, Band gap, effective masses, and energy level alignment of 2D and 3D halide perovskites and heterostructures using DFT-1/2, Phys. Rev. Mater. **6**, 014604 (2022).

[81] P. Umari, E. Mosconi, and F. De Angelis, Infrared dielectric screening determines the low exciton binding energy of metal-halide perovskites, J. Phys. Chem. Lett. **9**, 620 (2018).

[82] P. O. Löwdin, A note on the quantum-mechanical perturbation theory, J. Chem. Phys. **19**, 1396 (1956).

[83] L. M. Roth, B. Lax, and S. Zwerdling, Theory of optical magneto-absorption effects in semiconductors, Phys. Rev. **114**, 90 (1959).

[84] H. Zhang, Z. Zhai, Z. Bi, H. Gao, M. Ye, Y. Xu, H. Tan, and L. Yang, Spin coherence and spin relaxation in hybrid organic-inorganic lead and mixed lead-tin perovskites, Nano Lett **23**, 7914 (2023).